THE JOURNAL OF PHYSICAL CHEMISTRY C

Article

pubs.acs.org/JPCC

Probing the Hydrophobic Interaction between Air Bubbles and Partially Hydrophobic Surfaces Using Atomic Force Microscopy

Chen Shi,[†] Derek Y. C. Chan,[‡,§] Qingxia Liu,[†] and Hongbo Zeng*[,†]

[†]Department of Chemical and Materials Engineering, University of Alberta, Edmonton, AB T6G 2V4, Canada

[‡]Department of Mathematics and Statistics, University of Melbourne, Parkville 3010, Australia

[§]Department of Chemistry and Biotechnology, Swinburne University of Technology, Hawthorn 3122, Australia

Supporting Information

ABSTRACT: The hydrophobic interaction plays an essential role in various natural phenomena and industrial processes. Previous studies on the hydrophobic interaction focused mainly on the interaction between hydrophobic solid surfaces for which the effective range of hydrophobic attraction was reported to vary from ~10 nm to >1 μm. Here, we report studies of the interaction between an air bubble in water used as a probe attached to the cantilever of an atomic force microscope and partially hydrophobized mica surfaces. No bubble attachment was observed for bare hydrophilic mica, but attachment behaviors and attraction with an exponential decay length of 0.8−1.0 nm were observed between the air bubble and partially hydrophobized mica as characterized by a water contact angle on the mica surface that varied from 45° to 85°. Our results demonstrate the important roles of the additional attraction at partially hydrophobized surfaces and hydrodynamic conditions in bubble attachment to substrate surfaces and provide new insights into the basic understanding of this interaction mechanism in various applications such as mineral flotation.

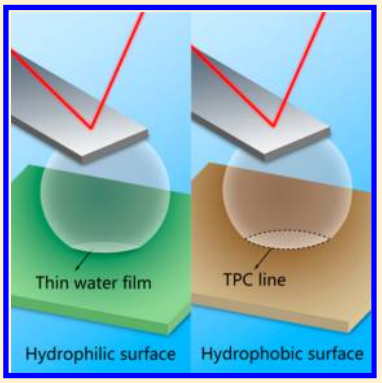

1. INTRODUCTION

The hydrophobic interaction between surfaces immersed in aqueous solutions refers to the additional long-range attraction that cannot be described by the classic Derjaguin−Landau−Verwey−Overbeek (DLVO) theory of colloidal stability.[1−3] This extra interaction plays a key role in a variety of natural phenomena and industrial processes, such as low solubility of nonpolar solutes in water,[4] coalescence of oil drops in aqueous solution,[4] formation of micelles,[4,5] self-assembly of hydrophobic nanoparticles,[6] protein folding,[4,7] and mineral flotation.[6,8−11] The basis of this interaction is generally attributed to an unfavorable entropy increase when nonpolar molecules that cannot form hydrogen bonding with water molecules disturb the configuration of the hydrogen bond network of nearby water molecules.[4,12,13] However, the detailed mechanism of the hydrophobic interaction as well as the precise range and magnitude of such interaction between extended surfaces is still under debate.[14,15]

Direct measurement of the interaction between self-assembled hydrophobic surfactant monolayers deposited on mica surfaces was first reported by Israelachvili and Pashley in 1982[3] and revealed that the hydrophobic interaction has a magnitude that is stronger than the attractive van der Waals (VDW) force and decays exponentially with a characteristic length of about 1 nm. Since then, much work has been done to measure the hydrophobic interaction between mica and silica surfaces that have been hydrophobized by adsorbed or chemically bonded layers of organic molecules.[16−20] The range of the hydrophobic interaction has been reported to vary from a few nanometers, which is normally considered as the "true hydrophobic force", up to hundreds of nanometers, which has been attributed to electrostatic interaction due to charged patches or capillary bridging due to interfacial nanobubbles.[21−26] The presence of interfacial submicroscopic nanobubbles is believed to be one of the major origins of long-range attraction between two hydrophobic surfaces[21−27] and long-range repulsion between the hydrophobic surface and hydrophilic surface.[28] Therefore, understanding the interaction mechanism between air bubbles and hydrophobic surfaces is important for elucidating the roles of nanobubbles and dissolved gases in hydrophobic interaction and their origin.[29]

The interaction between a large sessile air bubble on a substrate and a small solid spherical particle was measured with the atomic force microscope (AFM) using the colloidal probe technique in the 1990's.[30,31] The zero separation reference was deduced initially by treating the deformation of the air bubble as a Hookean spring with an effective spring constant equal to surface tension of water, although there have been subsequent refinements.[32−38] The surface forces apparatus (SFA) was also modified to measure the interaction force between an air bubble and a mica surface.[39,40] Recently, the AFM bubble probe method was developed and applied to investigate the interactions between two air bubbles and between an air bubble and hydrophilic surfaces (e.g., bare silica and mica

Received: July 17, 2014
Revised: August 31, 2014
Published: October 2, 2014

   dx.doi.org/10.1021/jp507164c | J. Phys. Chem. C 2014, 118, 25000−25008

surfaces). The interaction forces were successfully interpreted by theoretical modeling,[32,35−38,41,42] and it was shown that the repulsive VDW force could successfully prohibit bubble attachment onto these hydrophilic surfaces.[41] Very recently, hydrophobic interaction between two oil drops was measured, and a short-ranged attraction was reported.[43] Short-ranged hydrophobic attraction was also observed between the oil and bubble in aqueous solution.[44]

In this work, we report results of bubble probe AFM measurements of the interaction between an air bubble and mica surfaces that have been hydrophobized to different degrees in 0.5 M $NaNO_3$ solution. A theoretical model was applied to fit the force profiles under quasi-equilibrium conditions and was then used to predict the interactions under other hydrodynamic conditions. The results provide new insights into the basic understanding of the effects of air bubbles and dissolved gases in hydrophobic interaction and the origin of hydrophobic interactions.

2. EXPERIMENTAL METHODS AND THEORETICAL MODEL

2.1. AFM Measurement. High-purity sodium nitrate ($NaNO_3$) was used as received (Sigma-Aldrich, USA). The aqueous solution was prepared with Milli-Q water (Millipore deionized) with a resistance of ≥18.2 MΩ·cm. A MPF-3D AFM (Asylum Research, Santa Barbara, CA) mounted on a Nikon Ti−U inverted microscope was applied for the force measurements. A typical schematic of the experimental setup for measuring the interaction between an air bubble and a solid surface using the AFM is shown in Figure 1A. The interaction

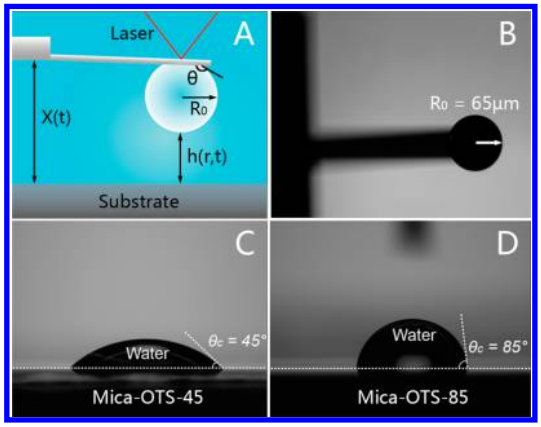

Figure 1. AFM experiment setup and contact angle images of hydrophobized mica surfaces. (A) Schematic of measuring the bubble−surface interaction by an AFM bubble probe, where the local separation (or film thickness), $h(r, t)$, between the air bubble and solid surface is a function of time t and radial coordinate r. (B) AFM bubble probe with bubble radius of 65 μm. (C) Water contact angle of ∼45° on the mica-OTS-45 surface. (D) Water contact angle of ∼85° on the mica-OTS-85 surface.

force is directly measured by monitoring the deflection of the cantilever by detecting the position of a laser beam reflected from the cantilever on a photodiode detector. Controlled variations of the actual position of the cantilever, $X(t)$, with time t, during a force measurement is measured and recorded with a linear variable differential transformer (LVDT) that is an integral part of the AFM. The corresponding interaction force $F(t)$ between the air bubble and the solid surface is also recorded. The thickness, $h(r, t)$, of the axisymmetric film between the air bubble and solid surface is calculated from a theoretical model (see section 2.3), where r is the radial coordinate.

Before measurements, the glass disk of an AFM fluid cell was treated in 10 mM OTS in toluene solution for ∼10 s to give a water contact angle of 30°−50° for better bubble immobilization. Air bubbles were carefully injected into the AFM fluid cell filled with 0.5 M $NaNO_3$ solution using a custom-made ultrasharp glass pipet. Custom-made rectangular silicon AFM cantilevers (400 × 70 × 2 μm) with a circular patch of gold (diameter 65 μm, thickness 30 nm) were used for anchoring the bubble securely on the cantilever. The gold patch was hydrophobized in 10 mM dedcanethiol in absolute ethanol overnight to form a hydrophobic area favorable for bubble attachment. The spring constants of the cantilevers were measured to be 0.3−0.4 N/m using the Hutter and Bechhoefer method.[45] A typical bubble probe was made by bringing down the cantilever to contact with a bubble of suitable size on the substrate and then carefully lifting the cantilever up. A picture of a prepared AFM bubble probe with bubble radius of 65 μm is shown in Figure 1B.

Interactions between the air bubble and hydrophobized mica surfaces were explored under different hydrodynamic conditions by varying the velocity, $dX(t)/dt$, of the air bubble attached to the force-sensing cantilever of the AFM. The interactions between bubble and surfaces under low velocities (i.e., 0.1 μm/s) were investigated to elucidate the effects of surface forces, under quasi-equilibrium condition with negligible hydrodynamic interaction. The effects of hydrodynamic interaction were then investigated at higher velocities (10−30 μm/s).

2.2. Hydrophobization of Mica Surfaces. Mica surfaces were hydrophobized through a vapor deposition process. Octadecyltrichlorosilane (OTS, ACROS Organics) was used as received. The freshly cleaved mica was exposed to OTS vapor for different durations at room temperature (23 °C) to achieve varying degrees of surface hydrophobicity characterized by different water contact angles θ_c, denoted as mica-OTS-45 (θ_c = 45°) and mica-OTS-85 (θ_c = 85°) as shown in Figure 1C and 1D, respectively. The hydrophobized mica surfaces were washed with toluene, ethanol, and Milli-Q water sequentially before being used for force measurements. The morphology of the hydrophobized mica surfaces was investigated by AFM tapping mode imaging. Both surfaces show very low root-mean-square roughness ∼0.3 nm (see Supporting Information).

2.3. Theoretical Model. The Stokes−Reynolds−Young−Laplace model is applied to describe the bubble−substrate interaction, taking into account the deformation of an air bubble, which has been successfully applied to describe various cases of interaction involving air bubbles or oil drops.[32,35−38,42,43] The thinning behavior of $h(r,t)$ between the air bubble and solid surface is described by the Reynolds lubrication theory with immobile boundary conditions at air/water and water/substrate interfaces as[36,41,42,46−55]

$$\frac{\partial h}{\partial t} = \frac{1}{12\mu r}\frac{\partial}{\partial r}\left(rh^3\frac{\partial p}{\partial r}\right) \quad (1)$$

where μ is the viscosity of water and $p(r,t)$ is the excess hydrodynamic pressure relative to the bulk solution. It is noted that the interface between hydrophilic mica and water is generally believed to be immobile, while immobile boundary conditions have also been observed between smooth hydro-

dx.doi.org/10.1021/jp507164c | J. Phys. Chem. C 2014, 118, 25000−25008

phobic surface and water.[55] The tangentially immobile or no-slip hydrodynamic boundary conditions were applied for the air/water interface because recent experimental results on thin film drainage and AFM force measurements involving air bubbles support and agree with this boundary condition, and as we shall see, this boundary condition also gives predictions that agree well with our experimental data in this work.[36,41,42,46−55] In fact, theoretical predictions with a slip boundary condition would lead to much smaller hydrodynamic repulsion and early bubble attachment onto the solid surface (see Figure S2 in Supporting Information). The immobile boundary condition at the air/water interface is believed to result from a trace amount of airborne surface active impurity that is always present even under careful laboratory conditions,[48−51] which has been known to arrest boundary mobility even though the reduction of the interfacial tension by such trace impurities can be as small as 0.1 mN/m or less.[48,49] The effect of ion redistribution near the air/water interface in concentrated salt solution has also been suggested as the cause of interfacial immobility.[46]

Deformation of the air bubble during interaction due to hydrodynamic pressure and disjoining pressure is described by the augmented Young−Laplace equation as

$$\frac{\gamma}{r}\frac{\partial}{\partial r}\left(r\frac{\partial h}{\partial r}\right) = \frac{2\gamma}{R_0} - p - \Pi \tag{2}$$

where γ is the water−air interfacial tension; R_0 is the bubble radius; and $\Pi(h(r,t))$ is the disjoining pressure that includes the contributions of surface forces such as van der Waals (VDW) and electrical double-layer (ED) interactions.

The interaction force $F(t)$ is theoretically calculated by integrating excess hydrodynamic pressure $p(r,t)$ and disjoining pressure $\Pi(h(r,t))$ as shown in eq 3. The disjoining pressure between two flat surfaces (see section 2.4) was used here for integration to calculate the overall interaction force between the bubble and substrate surface based on an approach similar to the Derjaguin approximation (for calculating the interaction forces between two bodies of arbitrary shapes in terms of the disjoining pressure between two flat surfaces).

The force $F(t)$ is calculated using the expression

$$F(t) = 2\pi\int_0^\infty (p(r,t) + \Pi(h(r,t)))r\mathrm{d}r \tag{3}$$

by integrating over the interval $0 \le r \le r_{max}$, where most of the contribution to the interaction force F is included, as reported previously.[35−38,41,42,52] The value, r_{max}, was chosen to be large enough so that small change in r_{max} has a negligible effect on the calculated interaction force F.[35−38]

The boundary condition at $r = 0$ follows symmetry considerations: $\partial h/\partial r = 0$ and $\partial p/\partial r = 0$. Considering the incompressible volume of the air bubble during interaction and that the air bubble is anchored on the tipless cantilever with a pinned contact area, the boundary condition at $r = r_{max}$ takes the form[35−38,42,52]

$$\frac{\partial h(r_{max},t)}{\partial t} = \frac{dX(t)}{dt} + \frac{dF(t)}{2\pi\gamma dt}\left(\frac{2\pi\gamma}{K} - 1 - \frac{1}{2}\ln\left(\frac{1+\cos\theta}{1-\cos\theta}\right) - \ln\left(\frac{r_{max}}{2R_0}\right)\right) \tag{4}$$

where $X(t)$ is the position of the cantilever as shown in Figure 1A; K is the spring constant of the cantilever; and θ is the contact angle of the air bubble on the cantilever. Since the bubble is constrained on the hydrophobized circular gold patch with known radius r_{gold} on the cantilever, a pinned three-phase contact line is applied here, and θ can be calculated based on equation $\sin(180 - \theta) = r_{gold}/R_0$.[35−38] The decay of hydrodynamic excessive pressure follows r^{-4} for $r \to \infty$, which indicates the boundary condition $r(\partial p/\partial r) + 4p = 0$ at $r = r_{max}$.[35−38,56] The initial condition for the film thickness is derived from the undeformed bubble profile, taking the form $h(r,0) = h_0 + r^2/R_0$ where h_0 is the initial central separation between the air bubble and the substrate. The h_0 can be theoretically fitted,[35−38,41,42,52] and its validity has been verified with independent measurement by AFM-integrated confocal microscopy.[57]

All the equations above are first nondimensionalized with $h_c = R_0Ca^{1/2}$, $r_c = R_0Ca^{1/4}$, $p_c = \gamma/R_0$, and $t_c = \mu Ca^{-1/2}$, where $Ca = \mu V/\gamma$ is the capillary number, and then are solved numerically after central difference discretization in r with MATLAB. More details of the numerical method can be found in previous reports.[35−38]

2.4. Components of the Disjoining Pressure. As shown in eq 3, the overall interaction force is an integral of the excess hydrodynamic pressure $p(r,t)$ and disjoining pressure $\Pi(h(r,t))$ in the interaction region. Therefore, equations for the surface interactions that contribute to $\Pi(h(r,t))$ are needed in the theoretical calculations. In this work, the bubble−substrate interactions were investigated in concentrated 0.5 M $NaNO_3$ solution; therefore, the electrical double-layer interaction was significantly compressed, and its contribution $\Pi_{ED}(h(r,t))$ to $\Pi(h(r,t))$ was negligible. The disjoining pressure due to VDW interaction $\Pi_{VDW}(h(r,t))$ is calculated by applying the full Lifshitz theory,[58] which includes the electromagnetic retardation effect. Denoting the air bubble, substrate surface, and aqueous solution as 1, 2, and 3, respectively, $\Pi_{VDW}(h(r,t))$ is calculated as

$$\Pi_{VDW}(h(r,t)) = -\frac{dE(h(r,t))}{dh(r,t)} = -\frac{A(h(r,t))}{6\pi h(r,t)^3} + \frac{1}{12\pi h(r,t)^2}\frac{dA(h(r,t))}{dh(r,t)} \tag{5}$$

$$A(h(r,t)) = -\frac{3}{2}kT\sum_{n=1}^{\infty}{}'\int_{r_n}^{\infty} x\ln[(1-\Delta_{13}\Delta_{23}e^{-x}) \times (1-\bar{\Delta}_{13}\bar{\Delta}_{23}e^{-x})]\mathrm{d}x \tag{6}$$

$$\Delta_{ij} = \frac{\varepsilon_i s_j - \varepsilon_j s_i}{\varepsilon_i s_j + \varepsilon_j s_i},\quad \bar{\Delta}_{ij} = \frac{s_j - s_i}{s_j + s_i},\quad s_k = \sqrt{x^2 + \left(\frac{2\xi_n h(r,t)}{c}\right)^2(\varepsilon_k - \varepsilon_3)}$$

$$r_n = \frac{2h(r,t)\xi_n\sqrt{\varepsilon_3}}{c},\quad \xi_n = \frac{2\pi nkT}{\hbar},\quad \varepsilon_k = \varepsilon_k(i\xi_n)$$

where c is the speed of light in vacuum; k is the Boltzmann constant; T is the temperature; $\hbar$ is the Dirac constant; and $\varepsilon_k = \varepsilon_k(i\xi_n)$ is the dielectric permittivity. It is noted that the first term in eq 5 contributes most to Π_{VDW} and the second term is far less. The dielectric permittivity of water was taken from the

literature.[59] The dielectric permittivity of the mica substrate was constructed using a Cauchy plot with data from Anita et al.[60] The zero frequency ($n = 0$) term in eq 6 has been omitted due to screening at high salt concentration. The calculated Hamaker function and disjoining pressure can be found in the Supporting Information.

For the contribution of hydrophobic interaction to the disjoining pressure, denoted as $\Pi_{HB}(h(r,t))$, the exponential function reported by Israelachvili and Pashley[3,15,20] is applied for the hydrophobic disjoining pressure, Π_{HB}, as show in eq 7

$$\Pi_{HB}(h(r,t)) = -\frac{C}{2\pi D_0}\exp(-h(r,t)/D_0) \quad (7)$$

where C is a constant (with unit N/m) and D_0 is a characteristic decay length. From thermodynamic consideration, the interaction energy per unit area of two planar half-spaces in water should approach their work of adhesion, as the separation D decreases to 0. Therefore, the constant C is given by

$$(C/2\pi) = \gamma_{13} + \gamma_{23} - \gamma_{12} \quad (8)$$

where "1", "2", and "3" refer to air, surface, and aqueous solution, respectively. According to Young's equation $\gamma_{12} = \gamma_{23} + \gamma_{13}\cos\theta_c$, where θ_c is the water contact angle on the surface, so the constant C can be expressed as

$$C = 2\pi\gamma_{13}(1 - \cos\theta_c) \quad (9)$$

Therefore, the total disjoining pressure $\Pi(h(r,t))$ is given by eq 10, in which $\Pi_{ED}(h(r,t))$ is negligible due to the significantly suppressed electrical double-layer interaction

$$\Pi(h(r,t)) = \Pi_{VDW}(h(r,t)) + \Pi_{ED}(h(r,t)) + \Pi_{HB}(h(r,t)) \quad (10)$$

3. RESULTS AND DISCUSSION

3.1. Interaction between the Air Bubble and Hydrophilic Mica Surface. The interaction between the bubble and a hydrophilic mica surface was investigated under low velocity (0.1 μm/s) in a quasi-equilibrium state with negligible hydrodynamic interaction in order to understand the effects of surface forces. For the hydrophilic mica surface, the VDW interaction calculated based on the full Lifshitz model[58] is repulsive at all separations, implying that a stable thin water film will be maintained between the air bubble and the hydrophilic mica surface.[1] The open square symbols in Figure 2 show the measured force between the hydrophilic mica surface and an air bubble of radius 80 μm with nominal driving velocity of 0.1 μm/s. The solid curve shows the theoretical prediction based on Reynolds lubrication theory coupled with the augmented Young–Laplace equation. The inset in Figure 2A shows the theoretically calculated bubble profile at maximum force load, of which the central part of the air bubble is flattened and a thin water film is confined between the bubble and mica. Since the hydrodynamic force is negligible compared with surface forces, this thin water film is stabilized by the repulsive VDW force, and the thickness (h_{min}) is calculated to be 6.4 nm, where the VDW disjoining pressure is about 1800 Pa, equal to the Laplace pressure $2\gamma/R$ of bubble with bubble–water interfacial tension γ = 72.1 mN/m. During retraction, the thickness of the thin water film remains almost constant, but the flattened area shrinks before the bubble is pulled away. The results in Figure 2A demonstrate that the DLVO model is sufficient to describe the surface interaction between the bubble and hydrophilic mica in water, and the repulsive VDW force is strong enough to inhibit bubble attachment to bare mica.

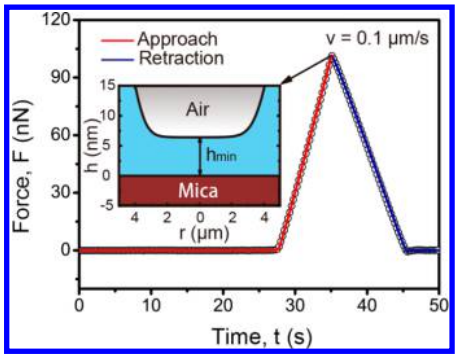

Figure 2. Force curve between an air bubble of radius 80 μm and the bare mica surface in 0.5 M $NaNO_3$ aqueous solution with nominal velocity of 0.1 μm/s. The open circle symbols are the experimental results, and the solid curves are the theoretically calculated forces. The inset shows calculated bubble profile at maximum force load at the point indicated by an arrow.

3.2. Interaction between an Air Bubble and the Hydrophobized Mica Surface. Figures 3A and 3D show the measured force curves between an air bubble and mica-OTS-45 and mica-OTS-85, respectively, in 0.5 M $NaNO_3$ solution with nominal velocity of 0.1 μm/s. Force curves in both figures show sudden "jump-in" behavior during the approach where the interaction force drastically turns from positive (repulsion) to negative (attraction), and strong adhesion is also observed during retraction. The jump-in behaviors indicate attachment of the air bubble onto the substrate surface, forming an air capillary bridge between the cantilever and the substrate that leads to the appearance of a strong attractive force. The inset schematics in Figures 3A and 3D illustrate estimated states of air bubble during the interaction. In both cases, the air bubbles are first slightly deformed due to the repulsive VDW and hydrodynamic forces and then suddenly attach to the hydrophobized mica surfaces, forming a three-phase contact line. As shown in Figure 3A, for mica-OTS-45, with water contact angle of ~45°, after bubble attachment, the net force could change from attractive to repulsive (viz. showing a second rise) during the continuous approach that results in a compression of the bubble. The observed repulsive force was mainly due to surface deformation of the bubble. For mica-OTS-85, with water contact angle of ~85°, a strong attraction could be detected instantaneously after bubble attachment due to the deformation of the bubble as shown in Figure 3D. For both cases, the bubble could not be detached from the mica surface by the cantilever during retraction, showing strong adhesion to the hydrophobized mica surfaces. Indeed, spontaneous detachment of bubble from the cantilever occurs occasionally for the mica-OTS-85 case during retraction. The stronger capillary adhesion for the bubble on mica-OTS-85 than that on mica-OTS-45 was simply due to the higher water contact angle on mica-OTS-85 and consequently larger bubble–mica contact area right after the bubble attachment during force measurement.

To model the interaction processes, the surface forces involved are first analyzed. As reported previously, the thickness of the coated self-assembled OTS layer is less than 1 nm, and the effects of the OTS coating on VDW interaction can be neglected at surface separation $D \geq 2$ nm.[1,61] Therefore, in this

dx.doi.org/10.1021/jp507164c | J. Phys. Chem. C 2014, 118, 25000–25008

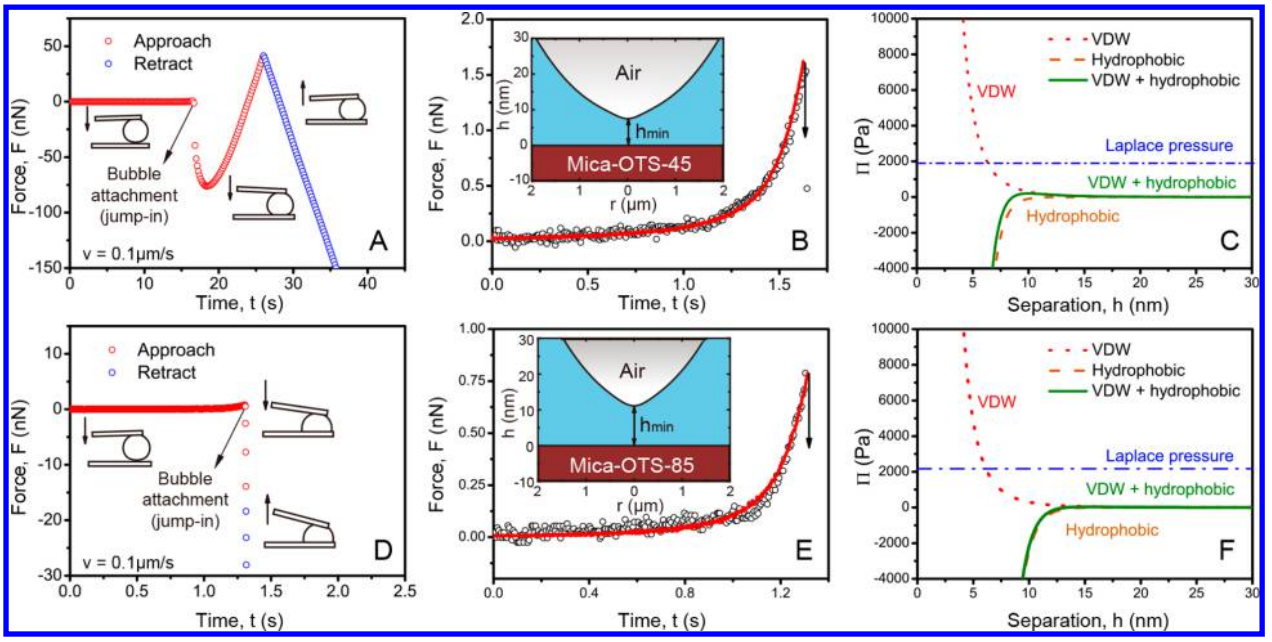

Figure 3. Measured and fitted force curves between a bubble approaching hydrophobized mica surfaces in 0.5 M $NaNO_3$ aqueous solution with nominal velocity of 0.1 μm/s prior to bubble attachment and calculated disjoining pressure between the bubble and hydrophobized mica surface. The open circle symbols are experimental results, and the solid curves are fitted force curves. The insets show the calculated bubble profile just before attachment. (A) Experimental force curve between an air bubble with radius of 80 μm and mica-OTS-45. (B) Fitted force curve between bubble of radius 80 μm and mica-OTS-45. (C) Calculated disjoining pressure profile for bubble and mica-OTS-45 in 0.5 M $NaNO_3$ solution. (D) Experimental force curve between an air bubble with radius of 65 μm and the mica-OTS-85 surface. (E) Fitted force curve between a bubble of radius of 65 μm and mica-OTS-85. (F) Calculated disjoining pressure profile for bubble and mica-OTS-85 in 0.5 M $NaNO_3$ solution.

work, the VDW interaction is taken to be that of the air−water−mica system, which is repulsive at any separation as described above. As the experiments were conducted in 0.5 M $NaNO_3$ solution, the electrical double layer was strongly suppressed, and the electrical double-layer interaction could be neglected in this system. An attractive interaction, namely, hydrophobic interaction, eqs 7−9, was added to the classical DLVO model to account for interaction with the hydrophobized mica. The observed "jump-in" behavior of the air bubble onto mica surfaces of different hydrophobicity can be accounted for by this additional term.

Eqs 7−9 describing the attractive hydrophobic interaction were incorporated in the theoretical model to describe the interactions between the air bubble and hydrophobized mica surfaces, mica-OTS-45 and mica-OTS-85. The constant C in eqs 7−9 was calculated to be 0.13 and 0.41 N/m for mica-OTS-45 and mica-OTS-85. By fitting the force curves at 0.1 μm/s, the decay length D_0 was determined to be 0.8 ± 0.1 nm and 1.0 ± 0.1 nm for mica-OTS-45 and mica-OTS-85, respectively. Figure 3B and 3E show the theoretical fitting results (solid curves), and the insets show the calculated bubble profile right before bubble attachment. The calculated bubble shape in the inset of Figure 3B shows that the center region of the bubble is more strongly attracted to the mica-OTS-45 surface due to the attractive hydrophobic interaction, and the minimum water film thickness h_{min} before the "jump-in" was calculated to be 7.5 nm. The calculated disjoining pressure for the mica-OTS-45 case is also shown in Figure 3C, which clearly indicates that hydrophobic interaction plays the most critical role in bubble attachment to the hydrophobized mica surface. Similar results for the mica-OTS-85 are shown in Figures 3E and 3F, in which the constant C was taken as 0.41 N/m, and the decay length D_0 fitted to be 1.0 ± 0.1 nm, and the critical film thickness h_{min} calculated to be ∼10 nm. It is also evident from Figure 3C and 3F that h_{min} is the critical distance where the overall disjoining pressure just exceeds the Laplace pressure of the bubble. The calculated disjoining pressure profiles also clearly show that the hydrophobic attraction between the bubble and mica-OTS-85 decays slower and is stronger than that of mica-OTS-45, consistent with the fact that mica-OTS-85 has a larger water contact angle of 85° as compared to 45° of mica-OTS-45.

3.3. Effects of Hydrodynamic Conditions. During interaction, higher approaching velocity of the bubble leads to stronger hydrodynamic interactions between the bubble and surface and different bubble attachment behaviors. The effects of hydrodynamic conditions were investigated by controlling the movement of the cantilever. The fitted decay length D_0 obtained under quasi-equilibrium conditions (viz., low velocity) was applied to predict the interactions of air bubble and mica-OTS-85 surface under different hydrodynamic conditions at higher velocities that were then compared with the experimental results.

Figure 4A shows the experimental results (open symbols) and predicted force profile (solid curve) for approach and retraction of a bubble against mica-OTS-85 with a nominal velocity of 30 μm/s and a maximum normal load of 20 nN. Figure 4B shows similar results with the same velocity but a larger maximum normal load of 50 nN. In both cases, the motion of the cantilever was changed from approach to retract after reaching the maximum load. In contrast, the results in Figure 4C correspond to the case that the air bubble first approached the mica-OTS-85 surface at 10 μm/s and was then stopped after reaching the maximum normal load of 8 nN. It is evident from Figure 4 that all the theoretical predictions with the thermodynamically determined constant C and fitted D_0 at the quasi-equilibrium state agree very well with the

dx.doi.org/10.1021/jp507164c | J. Phys. Chem. C 2014, 118, 25000−25008

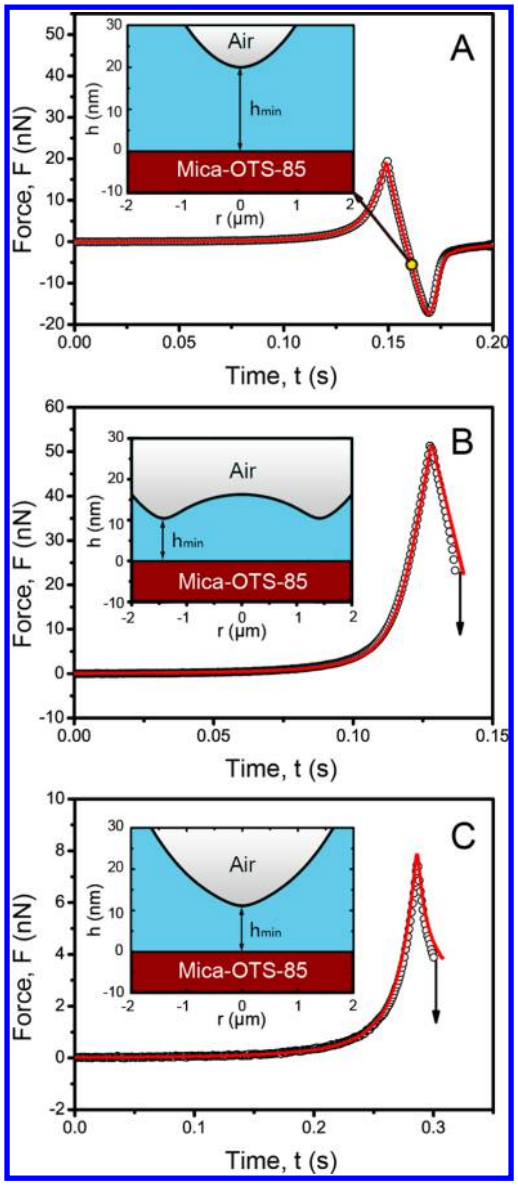

Figure 4. Predicted force curves of air bubble and mica-OTS-85 in 0.5 M $NaNO_3$ aqueous solution under different hydrodynamic conditions. The symbols are experimental results, and the solid curves are calculated force curves for theory. The insets show the calculated bubble profiles when the water film thickness is minimum. For all the figures, the decay length D_0 used is 1.0 ± 0.1 nm. (A) Force curve with nominal velocity of 30 μm/s and maximum normal load of 20 nN. No attachment occurred. (B) Force curve with nominal velocity of 30 μm/s and maximum normal load of 50 nN. Bubble attachment occurred during retraction. (C) Force curve with nominal velocity of 10 μm/s and maximum normal load of 8 nN. The cantilever was stopped after reaching the maximum load, and bubble attachment occurred after the cantilever was stopped.

experimental results at higher velocities. In Figure 4A the higher velocity 30 μm/s (as compared to 0.1 μm/s in Figure 3C) leads to stronger hydrodynamic repulsion that prevented the water film from draining to the thickness where hydrophobic interaction dominates, and thus no attachment is observed. The inset in Figure 4A shows the bubble profile when the separation is at its minimum, and the h_{min} is calculated to be 20 nm, where the hydrophobic force is too weak to induce water film rupture. It should be noted that the minimal separation is achieved not at maximum force load but at some point during retraction, indicated by the arrow in Figure 4A, which is due to the hydrodynamic "suction" effect.[17,18] For Figure 4B, with the increased maximum load of 50 nN, the extent of bubble deformation is larger which traps a larger water film between the bubble and the hydrophobized mica surface. Interestingly, attachment does not occur during approach but during retraction of the bubble due to the hydrodynamic suction effect that draws the bubble closer to the mica surface and within range of the hydrophobic attraction that causes rupture of the water film. The bubble also exhibits a "dimple" shape as shown in the inset of Figure 4B, indicating that the thinnest part of the water film locates at a rim region near the center (~10 nm) before attachment. In Figure 4C upon stopping the cantilever (and bubble), the hydrodynamic repulsion releases quickly (<0.02 s), and the water film continues to drain which leads to the bubble attachment (with a similar bubble profile as that in Figure 3c with a nominal velocity of 0.1 μm/s).

To better understand the formation of the dimple in Figure 4B, the evolutions of thin film thickness and excess hydrodynamic pressure are shown in Figure 5. At time t = 0.120 s, the

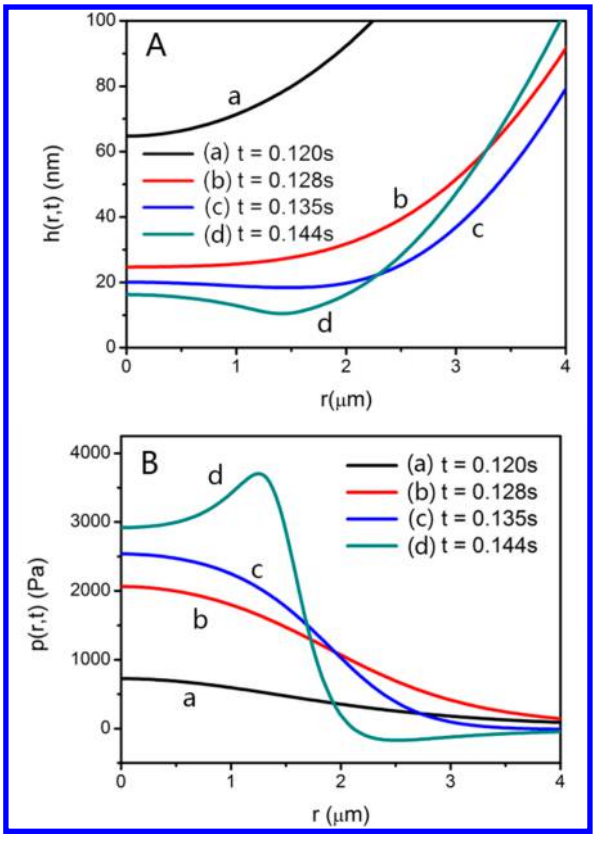

Figure 5. Calculated values of (A) the film thickness $h(r,t)$ and (B) hydrodynamic pressure $p(r,t)$ at different time corresponding to interaction in Figure 4B. (a) t = 0.120 s; (b) t = 0.128 s; (c) t = 0.135 s; (d) t = 0.144 s.

minimal separation between the air bubble and the surface was calculated to be 65 nm. At this separation, the excess hydrodynamic pressure increased but was still less than the Laplace pressure inside the air bubble, and thus the air bubble was slightly flattened in the central part accordingly. At time t = 0.128 s, the excess hydrodynamic pressure exceeded the Laplace pressure of the air bubble, which led to an inversion

dx.doi.org/10.1021/jp507164c | J. Phys. Chem. C 2014, 118, 25000−25008

of the curvature in the central part (see eq 2), and a dimple started to form. As the air bubble approached the substrate, the dimple further developed, with the expanding dimple rim and decreasing separation at the rim. At the minimal separation, which located at the dimple rim, the bubble surface and hydrophobized substrate reached the effective range of hydrophobic interaction (~10 nm here), and the hydrophobic attraction suddenly enhanced the local film thinning rate and thus led to bubble attachment onto the hydrophobized surface.

3.4. Implications on the Hydrophobic Interaction. Although hydrophobic interaction has been investigated for decades, the exact physical origin and mechanism of hydrophobic interaction is still under debate. It is commonly believed that the hydrophobic interaction should be related to the loss of hydrogen bonding between water molecules near the hydrophobic surface and thus increase entropy. Our experiment, for the first time, measured the hydrophobic interaction in an asymmetric system (viz., a deformable air bubble and a hydrophobic solid surface), which is inherently different from that of the symmetric interaction between solid surfaces or droplets.[32,35,36,38,42] The measured strength and decay length of the hydrophobic interaction (0.8−1 nm) agrees well with the previously reported decay lengths for solid surfaces, indicating that the exponential model of hydrophobic interaction, originally measured between solid surfaces, could be applicable to interactions between an air bubble and a hydrophobic solid substrate. However, it is noted that the decay length (0.8−1 nm) in this work is larger than that measured between two oil drops (~0.3 nm). Such disagreement might indicate different mechanisms of hydrophobic interaction at solid/water, air/water, and oil/water interfaces. The shorter decay length of ~0.3 nm possibly results from short-ranged water correlations at the oil/water or air/water interface, while the disruption of long-ranged dipolar, hydrogen bonding network and proton-hopping correlation at the solid/water interface could be attributed to the longer decay length of ~1 nm.[14,15] Therefore, when an air bubble interacts with a hydrophobic solid surface, the hydrophobic interaction could be dominated by the one with a longer decay length. It is also noted that our results show the hydrophobic interaction is significant for a partially hydrophobic surface with contact angle <90° (for hydrophobic bubble attachment), and the hydrophobic interaction decreases with decreasing surface hydrophobicity.

The measured hydrophobic attraction between an air bubble and the hydrophobic solid surface also provides thermodynamic implications for the existence of an air bubble on a hydrophobic surface, the VDW force between which is generally repulsive in water. The surface immobilized nano- and microbubbles, which could form "externally" due to trapped air when contacting with water or "internally" from the water-dissolved gas, could be attributed to the reported long-range hydrophobic interaction between two solid surfaces.[17,22,24,28]

4. CONCLUSIONS

By directly probing the interaction force between air bubbles and hydrophobized mica surfaces in 0.5 M $NaNO_3$ solution, we demonstrate the important roles of hydrophobic interaction and hydrodynamic conditions in bubble attachment to substrate surfaces for the first time. No bubble attachment was observed for bare hydrophilic mica, but attachment behaviors and attraction with an exponential decay length of 0.8−1.0 nm were observed between an air bubble and partially hydrophobized mica with water contact angles varied from 45° to 85°. The strength of the hydrophobic interaction increases with an increase in water contact angle of the substrate. For a fixed hydrophobized mica surface, hydrodynamic interaction appears stronger with increasing bubble velocity, and bubble attachment can occur during bubble retraction instead of approach due to the hydrodynamic suction effect. Our results provide valuable information for a better understanding of the hydrophobic interaction and show implications in various applications where bubbles are involved such as mineral flotation.

■ ASSOCIATED CONTENT

Supporting Information

Details of experimental, analysis, and modeling protocols. This material is available free of charge via the Internet at http://pubs.acs.org.

■ AUTHOR INFORMATION

Corresponding Author

*E-mail: hongbo.zeng@ualberta.ca. Phone: +1-780-492-1044. Fax: +1-780-492-2881.

Notes

The authors declare no competing financial interest.

■ ACKNOWLEDGMENTS

This work was supported by the Natural Sciences and Engineering Research Council of Canada (NSERC), the Canada Foundation for Innovation (CFI), the Alberta Advanced Education & Technology Small Equipment Grants Program (AET/SEGP), and the Australian Research Council.

■ REFERENCES

(1) Israelachvili, J. N. *Intermolecular and Surface Forces*; revised 3rd ed.; Academic press: New York, 2011.

(2) Craig, V.; Ninham, B.; Pashley, R. Direct Measurement of Hydrophobic Forces: A Study of Dissolved Gas, Approach Rate, and Neutron Irradiation. *Langmuir* **1999**, *15*, 1562−1569.

(3) Israelachvili, J.; Pashley, R. The Hydrophobic Interaction Is Long-Range, Decaying Exponentially with Distance. *Nature* **1982**, *300*, 341−342.

(4) Meyer, E. E.; Rosenberg, K. J.; Israelachvili, J. Recent Progress in Understanding Hydrophobic Interactions. *Proc. Natl. Acad. Sci. U.S.A.* **2006**, *103*, 15739−15746.

(5) Christenson, H. K.; Claesson, P. M. Direct Measurements of the Force between Hydrophobic Surfaces in Water. *Adv. Colloid Interface Sci.* **2001**, *91*, 391−436.

(6) Sanchez-Iglesias, A.; Sanchez-Iglesias, A.; Grzelczak, M.; Altantzis, T.; Goris, B.; Perez-Juste, J.; Bals, S.; Van Tendeloo, G.; Donaldson, S. H., Jr.; Chmelka, B. F.; Israelachvili, J. N.; et al. Hydrophobic Interactions Modulate Self-Assembly of Nanoparticles. *ACS Nano* **2012**, *6*, 11059−11065.

(7) Dyson, H. J.; Wright, P. E.; Scheraga, H. A. The Role of Hydrophobic Interactions in Initiation and Propagation of Protein Folding. *Proc. Natl. Acad. Sci. U.S.A.* **2006**, *103*, 13057−13061.

(8) Duan, H. W.; Wang, D. Y.; Kurth, D. G.; Mohwald, H. Directing Self-Assembly of Nanoparticles at Water/Oil Interfaces. *Angew. Chem., Int. Ed.* **2004**, *43*, 5639−5642.

(9) Nguyen, A. V.; Schulze, H. J.; Ralston, J. Elementary Steps in Particle-Bubble Attachment. *Int. J. Miner. Process.* **1997**, *51*, 183−195.

(10) Schubert, H. Nanobubbles, Hydrophobic Effect, Heterocoagulation and Hydrodynamics in Flotation. *Int. J. Miner. Process.* **2005**, *78*, 11−21.

(11) Ralston, J.; Fornasiero, D.; Hayes, R. Bubble-Particle Attachment and Detachment in Flotation. *Int. J. Miner. Process.* **1999**, *56*, 133−164.
(12) Mezger, M.; Reichert, H.; Schoeder, S.; Okasinski, J.; Schroeder, H.; Dosch, H.; Palms, D.; Ralston, J.; Honkimaki, V. High-Resolution in Situ X-Ray Study of the Hydrophobic Gap at the Water-Octadecyl-Trichlorosilane Interface. *Proc. Natl. Acad. Sci. U.S.A.* **2006**, *103*, 18401−18404.
(13) Doshi, D. A.; Watkins, E. B.; Israelachvili, J. N.; Majewski, J. Reduced Water Density at Hydrophobic Surfaces: Effect of Dissolved Gases. *Proc. Natl. Acad. Sci. U.S.A.* **2005**, *102*, 9458−9462.
(14) Hammer, M. U.; Anderson, T. H.; Chaimovich, A.; Shell, M. S.; Israelachvili, J. The Search for the Hydrophobic Force Law. *Faraday Discuss.* **2010**, *146*, 299−308.
(15) Donaldson, S. H.; Røyne, A.; Kristiansen, K.; Rapp, M. V.; Das, S.; Gebbie, M. A.; Lee, D. W.; Stock, P.; Valtiner, M.; Israelachvili, J. Developing a General Interaction Potential for Hydrophobic and Hydrophilic Interactions. *Langmuir* **2014**, DOI: 10.1021/la502115g.
(16) Pashley, R. M.; McGuiggan, P. M.; Ninham, B. W.; Evans, D. F. Attractive Forces between Uncharged Hydrophobic Surfaces - Direct Measurements in Aqueous-Solution. *Science* **1985**, *229*, 1088−1089.
(17) Christenson, H. K.; Claesson, P. M. Cavitation and the Interaction between Macroscopic Hydrophobic Surfaces. *Science* **1988**, *239*, 390−392.
(18) Tsao, Y. H.; Evans, D. F.; Wennerstrom, H. Long-Range Attractive Force between Hydrophobic Surfaces Observed by Atomic-Force Microscopy. *Science* **1993**, *262*, 547−550.
(19) Lin, Q.; Meyer, E. E.; Tadmor, M.; Israelachvili, J. N.; Kuhl, T. L. Measurement of the Long- and Short-Range Hydrophobic Attraction between Surfactant-Coated Surfaces. *Langmuir* **2005**, *21*, 251−255.
(20) Donaldson, S. H., Jr.; Das, S.; Gebbie, M. A.; Rapp, M.; Jones, L. C.; Roiter, Y.; Koenig, P. H.; Gizaw, Y.; Israelachvili, J. N. Asymmetric Electrostatic and Hydrophobic-Hydrophilic Interaction Forces between Mica Surfaces and Silicone Polymer Thin Films. *ACS Nano* **2013**, *7*, 10094−10104.
(21) Considine, R. F.; Hayes, R. A.; Horn, R. G. Forces Measured between Latex Spheres in Aqueous Electrolyte: Non-DLVO Behavior and Sensitivity to Dissolved Gas. *Langmuir* **1999**, *15*, 1657−1659.
(22) Carambassis, A.; Jonker, L. C.; Attard, P.; Rutland, M. W. Forces Measured between Hydrophobic Surfaces Due to a Submicroscopic Bridging Bubble. *Phys. Rev. Lett.* **1998**, *80*, 5357−5360.
(23) Singh, S.; Houston, J.; van Swol, F.; Brinker, C. J. Superhydrophobicity - Drying Transition of Confined Water. *Nature* **2006**, *442*, 526−526.
(24) Faghihnejad, A.; Zeng, H. Hydrophobic Interactions between Polymer Surfaces: Using Polystyrene as a Model System. *Soft Matter* **2012**, *8*, 2746−2759.
(25) Zhang, X.; Chan, D. Y. C.; Wang, D.; Maeda, N. Stability of Interfacial Nanobubbles. *Langmuir* **2013**, *29*, 1017−1023.
(26) Yang, J. W.; Duan, J. M.; Fornasiero, D.; Ralston, J. Very Small Bubble Formation at the Solid-Water Interface. *J. Phys. Chem. B* **2003**, *107*, 6139−6147.
(27) Meagher, L.; Craig, V. S. J. Effect of Dissolved-Gas and Salt on the Hydrophobic Force between Polypropylene Surfaces. *Langmuir* **1994**, *10*, 2736−2742.
(28) Faghihnejad, A.; Zeng, H. Interaction Mechanism between Hydrophobic and Hydrophilic Surfaces: Using Polystyrene and Mica as a Model System. *Langmuir* **2013**, *29*, 12443−12451.
(29) Meyer, E. E.; Lin, Q.; Israelachvili, J. N. Effects of Dissolved Gas on the Hydrophobic Attraction between Surfactant-Coated Surfaces. *Langmuir* **2005**, *21*, 256−259.
(30) Ducker, W. A.; Xu, Z. G.; Israelachvili, J. N. Measurements of Hydrophobic and DLVO Forces in Bubble-Surface Interactions in Aqueous-Solutions. *Langmuir* **1994**, *10*, 3279−3289.
(31) Preuss, M.; Butt, H. J. Direct Measurement of Particle-Bubble Interactions in Aqueous Electrolyte: Dependence on Surfactant. *Langmuir* **1998**, *14*, 3164−3174.
(32) Dagastine, R. R.; Manica, R.; Carnie, S. L.; Chan, D. Y. C.; Stevens, G. W.; Grieser, F. Dynamic Forces between Two Deformable Oil Droplets in Water. *Science* **2006**, *313*, 210−213.
(33) Attard, P.; Miklavcic, S. J. Effective Spring Constant of Bubbles and Droplets. *Langmuir* **2001**, *17*, 8217−8223.
(34) Attard, P.; Miklavcic, S. J. Effective Spring Constant of Bubbles and Droplets (Vol 17, Pg 8217, 2001). *Langmuir* **2003**, *19*, 2532−2532.
(35) Manica, R.; Connor, J. N.; Dagastine, R. R.; Carnie, S. L.; Horn, R. G.; Chan, D. Y. C. Hydrodynamic Forces Involving Deformable Interfaces at Nanometer Separations. *Phys. Fluids* **2008**, *20*.
(36) Chan, D. Y. C.; Klaseboer, E.; Manica, R. Film Drainage and Coalescence between Deformable Drops and Bubbles. *Soft Matter* **2011**, *7*, 2235−2264.
(37) Chan, D. Y. C.; Klaseboer, E.; Manica, R. Theory of Non-Equilibrium Force Measurements Involving Deformable Drops and Bubbles. *Adv. Colloid Interface Sci.* **2011**, *165*, 70−90.
(38) Tabor, R. F.; Grieser, F.; Dagastine, R. R.; Chan, D. Y. C. Measurement and Analysis of Forces in Bubble and Droplet Systems Using AFM. *J. Colloid Interface Sci.* **2012**, *371*, 1−14.
(39) Pushkarova, R. A.; Horn, R. G. Bubble-Solid Interactions in Water and Electrolyte Solutions. *Langmuir* **2008**, *24*, 8726−8734.
(40) Pushkarova, R. A.; Horn, R. G. Surface Forces Measured between an Air Bubble and a Solid Surface in Water. *Colloids Surf., A* **2005**, *261*, 147−152.
(41) Tabor, R. F.; Manica, R.; Chan, D. Y. C.; Grieser, F.; Dagastine, R. R. Repulsive Van Der Waals Forces in Soft Matter: Why Bubbles Do Not Stick to Walls. *Phys. Rev. Lett.* **2011**, *106*.
(42) Vakarelski, I. U.; Manica, R.; Tang, X.; O'Shea, S. J.; Stevens, G. W.; Grieser, F.; Dagastine, R. R.; Chan, D. Y. C. Dynamic Interactions between Microbubbles in Water. *Proc. Natl. Acad. Sci. U.S.A.* **2010**, *107*, 11177−11182.
(43) Tabor, R. F.; Wu, C.; Grieser, F.; Dagastine, R. R.; Chan, D. Y. C. Measurement of the Hydrophobic Force in a Soft Matter System. *J. Phys. Chem. Lett.* **2013**, *4*, 3872−3877.
(44) Li, E. Q.; Vakarelski, I. U.; Chan, D. Y. C.; Thoroddsen, S. T. Stabilization of Thin Liquid Films by Repulsive Van Der Waals Force. *Langmuir* **2014**, *30*, 5162−5169.
(45) Hutter, J. L.; Bechhoefer, J. Calibration of Atomic-Force Microscope Tips. *Rev. Sci. Instrum.* **1993**, *64*, 1868−1873.
(46) Parkinson, L.; Ralston, J. The Interaction between a Very Small Rising Bubble and a Hydrophilic Titania Surface. *J. Phys. Chem. C* **2010**, *114*, 2273−2281.
(47) Manica, R.; Chan, D. Y. C. Drainage of the Air-Water-Quartz Film: Experiments and Theory. *Phys. Chem. Chem. Phys.* **2011**, *13*, 1434−1439.
(48) Yaminsky, V. V.; Ohnishi, S.; Vogler, E. A.; Horn, R. G. Stability of Aqueous Films between Bubbles. Part 2. Effects of Trace Impurities and Evaporation. *Langmuir* **2010**, *26*, 8075−8080.
(49) Yaminsky, V. V.; Ohnishi, S.; Vogler, E. A.; Horn, R. G. Stability of Aqueous Films between Bubbles. Part 1. The Effect of Speed on Bubble Coalescence in Purified Water and Simple Electrolyte Solutions. *Langmuir* **2010**, *26*, 8061−8074.
(50) Manor, O.; Chan, D. Y. C. Terminal Velocity and Mobile Surface Species in Rising Microbubbles. *Langmuir* **2009**, *25*, 8899−8902.
(51) Del Castillo, L. A.; Ohnishi, S.; White, L. R.; Carnie, S. L.; Horn, R. G. Effect of Disjoining Pressure on Terminal Velocity of a Bubble Sliding Along an Inclined Wall. *J. Colloid Interface Sci.* **2011**, *364*, 505−511.
(52) Manor, O.; Vakarelski, I. U.; Stevens, G. W.; Grieser, F.; Dagastine, R. R.; Chan, D. Y. C. Dynamic Forces between Bubbles and Surfaces and Hydrodynamic Boundary Conditions. *Langmuir* **2008**, *24*, 11533−11543.
(53) Tabor, R. F.; Chan, D. Y. C.; Grieser, F.; Dagastine, R. R. Anomalous Stability of Carbon Dioxide in Ph-Controlled Bubble Coalescence. *Angew. Chem., Int. Ed.* **2011**, *50*, 3454−3456.
(54) Hendrix, M. H. W.; Manica, R.; Klaseboer, E.; Chan, D. Y. C.; Ohl, C.-D. Spatiotemporal Evolution of Thin Liquid Films During

Impact of Water Bubbles on Glass on a Micrometer to Nanometer Scale. *Phys. Rev. Lett.* **2012**, *108*, 247803.
(55) Schaeffel, D.; Yordanov, S.; Schmelzeisen, M.; Yamamoto, T.; Kappl, M.; Schmitz, R.; Duenweg, B.; Butt, H.-J.; Koynov, K. Hydrodynamic Boundary Condition of Water on Hydrophobic Surfaces. *Phys. Rev. E* **2013**, *87*, 051001(R).
(56) Yiantsios, S. G.; Davis, R. H. On the Buoyancy-Driven Motion of a Drop Towards a Rigid Surface or a Deformable Interface. *J. Fluid Mech.* **1990**, *217*, 547−573.
(57) Tabor, R. F.; Lockie, H.; Mair, D.; Manica, R.; Chan, D. Y. C.; Grieser, F.; Dagastine, R. R. Combined AFM-Confocal Microscopy of Oil Droplets: Absolute Separations and Forces in Nanofilms. *J. Phys. Chem. Lett.* **2011**, *2*, 961−965.
(58) Ninham, B. W.; Parsegia, Va Vanderwaals Forces - Special Characteristics in Lipid-Water Systems and a General Method of Calculation Based on Lifshitz Theory. *Biophys. J.* **1970**, *10*, 646−663.
(59) Dagastine, R. R.; Prieve, D. C.; White, L. R. The Dielectric Function for Water and Its Application to Van Der Waals Forces. *J. Colloid Interface Sci.* **2000**, *231*, 351−358.
(60) Bailey, A. I.; Kay, S. M. Measurement of Refractive Index and Dispersion of Mica Employing Multiple Beam Interference Techniques. *Br. J. Appl. Phys.* **1965**, *16*, 39−44.
(61) Grabbe, A. Double-Layer Interactions between Silylated Silica Surfaces. *Langmuir* **1993**, *9*, 797−801.